PAPER

Check for updates

Structural evolution, optical gap and thermoelectric properties of CH₃NH₃SnBr₃ hybrid perovskite, prepared by mechanochemistry†

Carlos A. López,*[ab] Carmen Abia,[ac] Javier Gainza, [ID][a] Paula Kayser, [ID][a]
N. N. Nemes, [ID][ad] O. J. Dura, [ID][e] J. L. Martínez, [ID][a] María T. Fernández-Díaz,[c]
Consuelo Álvarez-Galván[f] and José A. Alonso [ID]*[a]

Direct bandgap semiconductors of the hybrid-perovskite family $CH_3NH_3PbX_3$ (X = I, Br, Cl) exhibit outstanding light absorption properties and are the materials of choice for solar energy applications. As an alternative to poisonous Pb, tin-containing perovskites would show a lower effective mass thus exhibiting a higher charge carrier mobility. An auspicious candidate is $CH_3NH_3SnBr_3$, with an estimated band gap of 1.902 eV, anticipating applications in photovoltaic devices for the visible to ultra-violet wavelength region. We describe that this perovskite can be prepared by ball milling in a straightforward way, yielding specimens with a superior crystallinity. A structural investigation from synchrotron X-ray powder diffraction (SXRD) data was essential to revisit the successive phase transitions this compound experiences down to 120 K, guided by specific heat capacity and DSC measurements. From the cubic structure identified at RT and 270 K, there is a gradual evolution of the patterns, analysed as a phase admixture between the cubic and the low-symmetry phase present at 160 K. This corresponds to an orthorhombic $Pmc2_1$ superstructure; this acentric space group enables polarization along the c-axis where there is a twofold screw axis, evidenced in the distribution of Sn–Br distances. Furthermore, there are two conspicuous changes in the orthorhombic framework, yet keeping the $Pmc2_1$ space group, which agree with the main calorimetric events (observed at 224 and 147 K). We interpret these changes as an interplay between the tilting of the $SnBr_6$ octahedra of the inorganic framework and the breaking and reconstruction of H-bond interactions with the organic $CH_3NH_3^+$ unit. The stereochemical effect of the lone electron pair of the Sn^{2+} ion is clear in the $SnBr_6$ octahedral distortion. Diffuse reflectance UV/Vis spectroscopy yields an optical gap of $\sim$2.1 eV, in agreement with *ab-initio* calculations. A Seebeck coefficient of $\sim$2000 µV K^{-1} is determined near RT, which is one order of magnitude higher than those reported for other halide perovskites.

[a] *Instituto de Ciencia de Materiales de Madrid, CSIC, Cantoblanco, 28049 Madrid, Spain. E-mail: ja.alonso@icmm.csic.es*

[b] *Instituto de Investigaciones en Tecnología Química (UNSL-CONICET) and Facultad de Química, Bioquímica y Farmacia, Almirante Brown 1455 (5700), San Luis, Argentina. E-mail: calopez@unsl.edu.ar*

[c] *Institut Laue Langevin, BP 156X, F-38042 Grenoble, France*

[d] *Departamento de Física de Materiales, Universidad Complutense de Madrid, E-28040 Madrid, Spain*

[e] *Departamento de Física Aplicada, Universidad de Castilla-La Mancha, Ciudad Real, E-13071, Spain*

[f] *Instituto de Catálisis y Petroleoquímica, CSIC, Cantoblanco, 28049 Madrid, Spain*

† Electronic supplementary information (ESI) available. See DOI: 10.1039/d1ma00196e

Introduction

Hybrid organic–inorganic halide perovskites have demonstrated applicability in photovoltaic technology,[1–6] with a power conversion efficiency (PCE) of about 23%, comparable to the best commercial silicon solar cells. The paradigmatic methylammonium lead iodide $CH_3NH_3PbI_3$ has thus emerged as a light harvester for hetero-junction solar cells.[7–9] Other direct bandgap semiconductors of the MAPbX₃ (MA = CH_3NH_3, X = I, Br, I) family exhibit properties such as outstanding light absorption, excellent ambipolar charge mobility, low exciton binding energy and tolerance to defects.[10–18] However, all of them contain poisonous lead, involving toxicity issues with potential public health problems.[19] Other divalent elements with a lower toxicity have been evaluated to replace Pb;[14,20–24] in particular, many different types of halides containing main group elements such as In(I,III), Sn(II,IV), Sb(III) and Bi(III) have also been studied for solar cell applications;[25] however, some of their crystal structures are quite different from the original ABX₃ type perovskite. This structural arrangement contains, in

its cubic aristotype phase, linear chains –B–X–B– that allow a perfect overlap of the p orbitals of the X and B atoms.[26–28]

Among the different candidates to replace Pb, the most auspicious one is Sn, since its materials possess narrowed optical band gaps and high optical absorption coefficients, given that Sn 5p orbitals are less dispersive than Pb 6p orbitals.[29,30] Regarding the effective mass of charge carriers, tin-based perovskites would show a lower magnitude than lead-based ones, and therefore Sn-based perovskites would exhibit a higher charge carrier mobility.[31] A particularly interesting material is the $CH_3NH_3SnBr_3$ perovskite, and closely related $CH_3NH_3SnX_3$ (X = halogen) derivatives. For an optimized $MASnI_{0.5}Br_{2.5}$ composition, a power conversion efficiency of 1.51% was demonstrated in liquid-junction PEC solar cells, with an increase of 20.8% with respect to $MASnI_3$ perovskites.[32] Recent *ab- initio* calculations[33] enabled the evaluation of a band gap of 1.902 eV for $CH_3NH_3SnBr_3$, anticipating applications in photovoltaic devices for the visible to ultra-violet wavelength region. Using UV-Vis measurements, the optical bandgap of films prepared by co-evaporation and sequential evaporation methods were determined to be 2.2–2.3 eV.[34] The estimated thermoelectric properties at room temperature also predict that $CH_3NH_3SnBr_3$ may be used in thermoelectric devices.[33] Recently, novel applications such as quaternary memories fabricated from $CH_3NH_3SnBr_3$ memcapacitors have been reported,[35] allowing high-density information storage due to their multilevel and adjustable capacitances and long-term retention without a power supply. Despite these interesting precursors, up to now there have been no experimental reports on transport properties such as electronic conductivity, the Seebeck coefficient or thermal transport. By contrast, in halide analogues such as $MAPbBr_3$ or $CsSnBr_3$, these properties have already been studied.[36,37]

Regarding the structural behavior, $CH_3NH_3SnBr_3$ has been described as cubic at room temperature (RT), space group $Pm\bar{3}m$ (#221), a = 5.903 Å,[38] and several phase transitions below RT have been detected by heat capacity measurements, unveiling four anomalies, at 46.0 K (of a displacive type), 188.2 K, 213.0 K, and 229.4 K (of an order–disorder type).[39] The transition entropies are consistent with the orientational disorder of the methylammonium ion in a cubic environment. Synchrotron X-ray powder diffraction (SXRD) data indeed reveal the existence of a phase between 230 and 188 K crystallizing in the $Pmc2_1$ space group, a = 5.8941(2), b = 8.3862(2), c = 8.2406(2) Å, driven by strong ferroelectric distortions of the octahedra, associated with the stereochemical activity of the Sn $5s^2$ lone pair.[40] The precise nature of a lower-temperature phase remains uncertain, although it appears likely to be triclinic.[40]

In this work, we present results on the structural evolution of $CH_3NH_3SnBr_3$ from temperature-dependent SXRD data in the 120–295 K interval, from a specimen prepared by ball milling with excellent crystallinity. In the cubic phase at RT, difference Fourier maps show that the methylammonium delocalization obtained differs from that observed in the lead-containing $CH_3NH_3PbBr_3$ perovskite phase, where the $CH_3NH_3^+$ unit is oriented along [100]. At 200 K we confirm the existence of a non-centrosymmetric $Pmc2_1$ phase that persists down to 120 K. The characterization of this ball-milled specimen is complemented with specific heat measurements,

UV-vis spectroscopy and scanning microscopy. Transport measurements reveal a Seebeck coefficient of $\sim$2000 µV K^{-1} near RT.

Experimental

$CH_3NH_3SnBr_3$ was synthesized in polycrystalline form by mechano-chemical synthesis (ball milling) from stoichiometric amounts of $SnBr_2$ and CH_3NH_3Br. The total mass of reactants was 1.5 g, which were weighed and mixed with 20 zirconia balls (5 mm diameter) in a N_2-filled glove-box. The reaction took place in a Retsch PM100 mill for 4 h at 400 rpm, in a sealed zirconia-lined jar under a N_2 atmosphere. Laboratory XRPD patterns were collected using a Bruker D5 diffractometer with $K_\alpha Cu$ (λ = 1.5418 Å) radiation. The thermal evolution of the crystallographic structure was studied by synchrotron X-ray powder diffraction (SXRD) at 120, 140, 160, 200, 221, 240, 270 and 298 K (room temperature). SXRD patterns were collected in high angular resolution mode (so-called MAD set-up) on the MSPD diffractometer in the ALBA synchrotron at Barcelona, Spain, selecting an incident beam with 38 keV energy, λ = 0.3252 Å.[41] The sample was contained in a 0.3 mm diameter quartz capillary that was rotating during the data acquisition. XRPD and SXRD patterns were analyzed with the Rietveld method using the FullProf program.[42,43] Heat capacity measurements were carried out in the range of 100 K to 300 K at different applied external magnetic fields (up to 9 T) in a PPMS system with a heat pulse method. Scanning Electron Microscopy (SEM) images were obtained using a Hitachi instrument, model TM-1000, coupled to an energy-dispersive X-ray spectrometer (EDX), working with an acceleration voltage of 15 kV and 60 s of acquisition time. The optical diffuse reflectance spectrum of the perovskite powder was measured at room temperature using a Varian Cary 5000 UV-VIS spectrophotometer.

The Seebeck coefficient was obtained by measuring simultaneously the drop voltages across the sample and a constantan reference wire with an electrometer (Keithley 6517B) and a nanovoltmeter (Keithley 2182A) under vacuum (10^{-3} mbar). The electrical resistivity was measured using an Agilent E4980A LCR meter. The total thermal conductivity was calculated from the thermal diffusivity (α) using Linseis LFA 1000 equipment, by the laser-flash technique. The thermal conductivity (κ) was determined using $\kappa = \alpha \cdot C_p \cdot d$, where C_p is the specific heat capacity and d is the sample density.

Results and discussion

The sample was obtained as a dark-red microcrystalline powder; the laboratory XRPD pattern at RT exhibits a cubic symmetry, in agreement with previous reports, indexable in the space group $Pm\bar{3}m$.[40,44] The crystal structure was confirmed through a Le-Bail fit in this space group, as displayed in Fig. S1 (ESI†), obtaining a unit-cell parameter a = 5.9595(1) Å.

Fig. S2 (ESI†) illustrates typical SEM images of the as-prepared $CH_3NH_3SnBr_3$ perovskite. Large particles with sharp edges and large surfaces are identified, mixed with smaller pieces with

less-defined shapes. The growth of large microcrystals, with tenths of microns as the maximal dimensions, is possible after 4 hours of ball milling reaction; this justifies the good crystallinity displayed in the diffraction patterns. The results from EDX analysis (Fig. S2c, ESI†) showed well-defined peaks corresponding to tin and bromine, with the determined weight% of these elements (Sn: 38.4 (33.12), Br: 61.6 (66.88)) in reasonable agreement with the nominal values (in parentheses).

The synchrotron pattern collected at RT confirms the cubic $Pm\bar{3}m$ space group were Sn^{2+} and Br^- ions are located in $1a$ (0,0,0) and $3d$ (0.5,0,0) Wyckoff sites. The $CH_3NH_3^+$ organic cation is centered at the (0.5,0.5,0.5) position. As is well known, in hybrid-perovskite structures, the methylammonium units can be delocalized along the [100], [110] or [111] directions.[45,46] In the present case, Difference Fourier Maps (DFM) from the calculated and observed electron density reveal that $CH_3NH_3^+$ is delocalized along the [100] direction. The final refinement using this model is illustrated in Fig. 1a and the main crystallographic results are listed in Table 1. Two views of the crystal structure and DFM are shown in Fig. 1b and c, respectively. The methylammonium delocalization obtained differs from that observed in the lead-counterpart phase, where it is lying along [110].[47] This difference is due to the smaller unit-cell size of the tin phase (a = 5.9038(1) Å) $vs.$ lead perovskite (for $CH_3NH_3PbBr_3$, a = 5.93076(2) Å), as expected considering the ionic radii of the inorganic cations ($r_{(Sn^{2+})}$ = 0.93 Å; $r_{(Pb^{2+})}$ = 1.19 Å).[48,49] This correlation between methylammonium alignment and unit-cell size also was observed in the $MAPbBr_{3-x}Cl_x$ series.[17]

Table 1 Crystallographic data for MASnBr₃ from the SXRD refinements at room temperature

System: cubic, Space group: $Pm\bar{3}m$, Z = 1. Unit-cell parameters: a = 5.9038(1) Å, and V = 205.78(1) Å³.

Atom		x	Y	z	U_{eq}	Occ.
Sn	$1a$	0	0	0	0.027(1)	1
Br	$3d$	0.5	0	0	0.099(1)	1
C	$6f$	0.639(2)	0.5	0.5	0.016(9)	0.166
N	$6f$	0.639(2)	0.5	0.5	0.016(9)	0.166
Anisotropic displacement parameters						
	U^{11}	U^{22}	U^{33}	U^{12}	U^{13}	U^{23}
Sn	0.027(1)	0.027(1)	0.027(1)	0	0	0
Br	0.044(1)	0.127(1)	0.127(1)	0	0	0
C/N	0.028(9)	0.010(8)	0.010(8)	0	0	0

R_p: 7.21%; R_{wp}: 8.98%; R_{exp}: 7.99%; χ^2: 1.26; R_{Bragg}: 4.47%.

On the other hand, low temperature synchrotron X-ray patterns were used to resolve the crystal structures below room temperature of this sample synthesized mechanochemically, taking into account the calorimetric behaviour analyzed from C_P and DSC measurements. The thermal evolution of C_P of the present sample is shown in Fig. 1d, showing a sharp peak at 224 K indicating a strong caloric process. Also, there are three additional anomalies at 147 (small peak), 273 (slope change) and 298 K (broad peak). This caloric behaviour is quite different from that reported previously in single-crystal samples growth from solution.[28,39] The present anomalies are less intense and the temperatures are shifted with respect to the values mentioned in the introduction. Considering the most defined peaks, it is
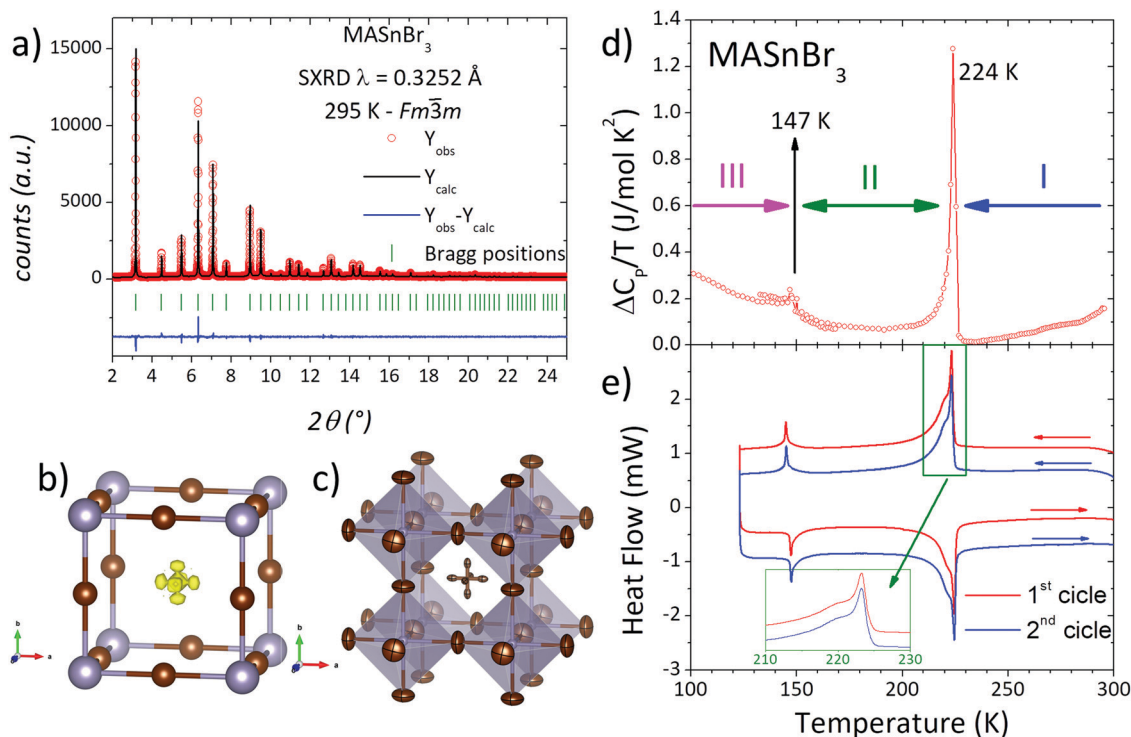

Fig. 1 (a) Observed (circles), calculated (full line) and difference (bottom) Rietveld profiles for MASnBr₃ from SXRPD data at RT. (b) Octahedral framework including Sn ad Br atoms, with DFM before MA incorporation. (c) Final cubic crystal structure after the Rietveld refinement at RT. (d) Heat capacity plotted as $\Delta C_P/T$ $vs.$ T. (e) First and second cycles of DSC curves. Inset shows an extended region of the most intense peak.

Paper

possible to accept the existence of three crystalline phases or states: $T > 224$ K, $147 > T > 224$ K and $T < 147$ K, labelled I, II and III, respectively in Fig. 1d. DSC measurements are shown in Fig. 1e. In excellent agreement with C_p data, the DSC curves display two main events at 144 and 223 K, confirming the three states mentioned previously. In addition, the greater resolution of DSC measurements allows observing a shoulder (centred at 220 K) over the main peak. Also, this signal could be deconvoluted into two peaks, where the most intense one is sharp and the shoulder is broad, as illustrated in Fig. 1e (inset). Moreover, DSC data also reveal the complete reversibility of the processes, showing that the second cycle perfectly matches with the first one.

To analyse these structural regions, additional SXRD patterns were collected at 270, 240, 221, 200, 160, 140 and 120 K. Fig. 2(a) plots the evolution of a selection of SXRD reflections, in particular corresponding to the cubic (100) and (220) planes, illustrating the structural changes at different temperatures. While the (100) plane shows no significant changes, the (220) reflection exhibits a conspicuous splitting, which indicates the presence of lower-symmetry phases below 240 K. This is also observed in other reflections, as complementarily shown in Fig. S3 (ESI†). The thermal evolution of the peak shape reveals that, at 270 K, the structure remains cubic, and a gradual change is observed from 240 to 160 K. Besides, the patterns at 140 and 120 K are similar to each other, but they are different from the remaining temperatures. These changes are in agreement with

the observed phase regions from calorimetric measurements: above 224 K, between 224 and 147 K and below 147 K, labelled in Fig. 1d as phases I, II and III, respectively.

The low-temperature crystal structure of $CH_3NH_3SnBr_3$ was first investigated in 1995 by Onoda-Yamamuro et al.[44] They reported this deuterated phase from neutron powder diffraction at 195 K as rhombohedral ($R\bar{3}c$). However, ten years ago, Swainson et al. reported the acentric $Pmc2_1$ space group in the 188–230 K temperature range from synchrotron powder diffraction and proposed a monoclinic acentric space group below 188 K.[40]

As mentioned above, from our SXRPD data we observe that the cubic symmetry remains when the sample is cooled down to 270 K, just showing the expected reduction in the unit-cell volume, while the methylammonium molecule remains aligned along the [100] direction. Fig. S4 and Table S1 (ESI†) show the Rietveld plots and the crystallographic results, respectively.

On the other hand, by analysing the gradual change mentioned above, it is evident that the patterns at 240, 221 and 200 K exhibit a phase mixture between the cubic and the low-symmetry phase present at 160 K. The two previously reported structures ($R\bar{3}c$ and $Pmc2_1$) were tested, finding a good agreement only with the orthorhombic $Pmc2_1$ space group, as it was previously reported by Swainson et al.[40] In this structural model, the unit-cell parameters are related to the cubic unit cell as $a_O \times \sqrt{2}a_O \times \sqrt{2}a_O$, with a_O being the aristotype cubic edge. Besides, the Sn^{2+} cation is located at $2a$ $(0,y,z)$ Wyckoff sites and Br^- anions are
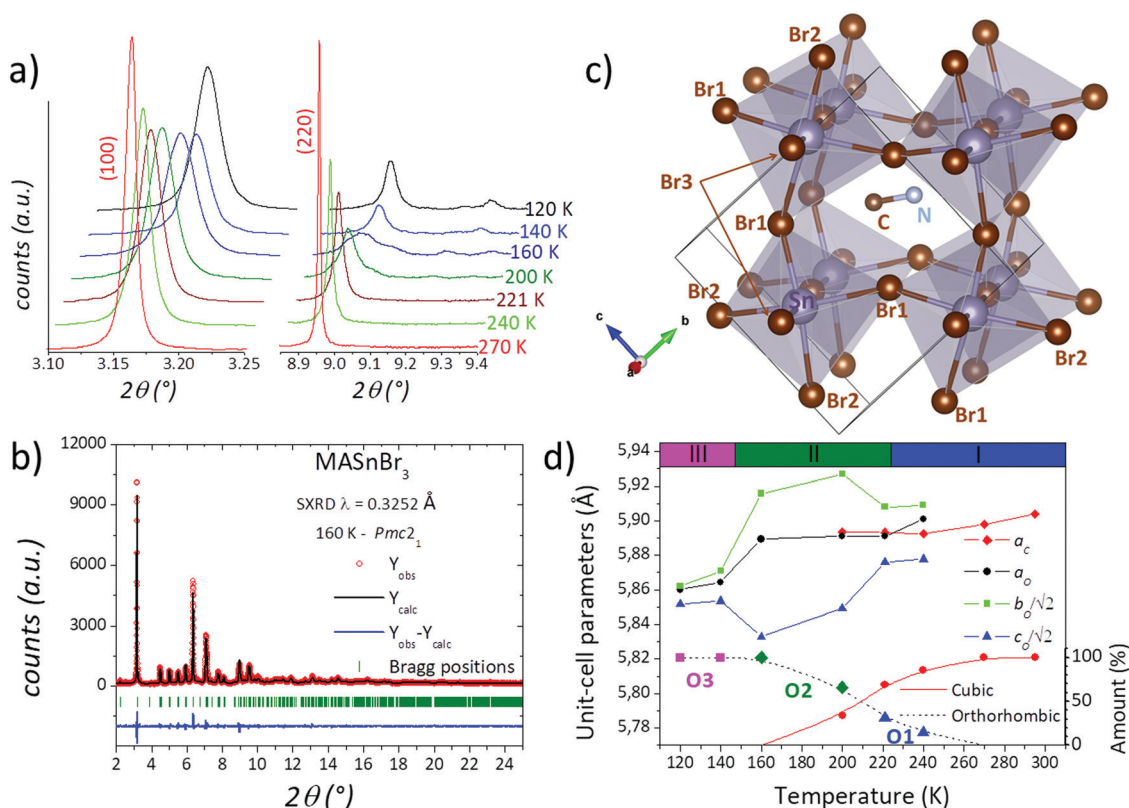

Fig. 2 (a) Thermal evolution of the (100) and (220) cubic lines from synchrotron diffraction. (b) Observed (circles), calculated (full line) and difference (bottom) Rietveld profiles for MASnBr₃ for SXRD data at 160 K. (c) Final crystal structure after Rietveld refinement at 160 K. (d) Evolution of the unit-cell parameters at different temperatures. The upper colour bars correspond to the calorimetric regions I, II and III.

distributed in two 2a and one 2b (0.5,y,z) sites. The C and N atoms are placed at 2b (0.5,y,z) sites, implying that the methyl-ammonium unit is localized within the (100) plane for x = 0.5. This model yields a good agreement after the Rietveld refinement, as plotted in Fig. 2b. The crystallographic results are listed in Table S2 (ESI†). This acentric space group enables a polarization along the c axis where there is a twofold screw axis. The polarization can be evidenced in the Sn–Br direction, where in the (100) plane there are two Sn–Br distances that are shorter than the other two. In addition, the MA is subtly tilted to the [100] direction in terms of the cubic polytype. These facts can be visualized in Fig. 2c. After resolving this structure in $Pmc2_1$ at 160 K, it was possible to refine the patterns at 240, 221 and 200 K, where a mixture of cubic and orthorhombic phases was found. The corresponding Rietveld plots are plotted in Fig. S5–S7 (ESI†), and the crystal data are listed in Tables S3–S5 (ESI†).

At lower temperatures, two patterns collected at 120 and 140 K are in the temperature range of phase III. Both patterns could also be properly fitted within the $Pmc2_1$ space group, but with a noticeably lower distortion with respect to the 160 K phase. This result contrasts with the triclinic models proposed by Swainson *et al.* for MASnBr₃ in this temperature range;[38] moreover, attempts to fit the patterns with these triclinic models were unsuccessful. It is remarkable that, despite the fact that the same $Pmc2_1$ space group can reliably define the crystal structure at 120 and 140 K, there are conspicuous differences with the 200 K structure; in particular the unit-cell parameters, $a_O \times \sqrt{2}b_O \times \sqrt{2}c_O$ are more similar to each other than those observed at 160 K. The Rietveld plots at these temperatures are shown in Fig. S8 and S9 (ESI†) and the crystallographic results are listed in Tables S6 and S7 (ESI†).

Therefore, four phases are identified, one cubic and three orthorhombic crystal structures, labelled: C, O1, O2 and O3, in addition to the mentioned mixture between C and O1 (and O2) phases in the 240–200 K range. The thermal evolution of the unit-cell parameters is illustrated in Fig. 2d, where the relative proportion of the four phases and the calorimetric regions are added. The first phase transition occurs in a broad temperature range of at least 50 K (from 250 to 200 K) where both cubic and orthorhombic structures coexist, contrasting with the previous results. Furthermore, there are two changes in the orthorhombic symmetry, which agree with the main calorimetric events (224 and 147 K). In addition, the subtle event at 270 K probably is due to the starting point of the phase transition from cubic to orthorhombic (O1) symmetry. These differences with respect to previous reports can be associated with the single crystal[38] *vs.* the polycrystalline state. The mechanochemical procedure generated a well-crystallized powder; however, this method also induces a strained grain surface, which probably modifies the thermal stability of the crystal structures.

In order to understand the three different structures with orthorhombic symmetry (O1, O2, O3) a careful analysis of selected bonds and angles has been carried out. The analysed parameters are: Sn–Br distances and Br–Sn–Br angles (to observe the SnBr₆ octahedral distortion) and the Sn–Br–Sn (to show the octahedral tilting). In addition, the angle between the MA and the ideal [100] direction was calculated, to estimate possible changes in H-bond interactions. These parameters are listed in Table S8, plotted in Fig. S10–S13 (ESI†) and schematized in crystal structure views in Fig. 3. The arrows on the Sn–Br1 and Sn–Br2 bonds indicate the longer (Sn–Br) distances in the equatorial plane of the SnBr₆ octahedron. The arrow on Br3 highlights its displacement along the c-axis with respect to the Sn atom. This distortion is sensitive to the Br3–Sn–Br3 angle, as listed in Table S8 (ESI†) and plotted in Fig. S12 (ESI†). In addition, the dashed line indicates the [100] direction (for the cubic polytype) to visualize the MA displacement.

These parameters show that the orthorhombic lattice undergoes gradual changes upon cooling down, as follows. Regarding the inorganic framework, the distortion starts at high temperature (240 and 221 K) with net polarization along the −c-axis, characterized by a low octahedral tilting. At 200 K the distortion in the equatorial plane of the octahedron changes to the b-axis and the tilts become greater. Then, at 160 K, the displacements return to the c direction and the tilt increases. At lower temperatures (120 and 140 K) the octahedral distortion and the tilts are greater, yielding a net polarization along the +c-axis. On the other hand, the organic MA molecules also evolve following the inorganic framework displacements or *vice versa*. At higher temperatures (240 and 221 K) the linear MA units are far from the [100] directions (see dashed line in Fig. 3a), but they approach the [100] line at 200 K, which is concomitant with the increase of the octahedral tilting (see Sn–Br–Sn angles, Fig. S12 and S13, ESI†). This change probably involves breaking and reconstructing H-bond interactions; these fluctuations involve strong enthalpy changes, in agreement with the intense signal observed in the heat capacity at 224 K (Fig. 1d). As mentioned above, this process in DSC presents a shoulder (Fig. 1e and inset), hence, considering both the organic and inorganic structural evolution in the lattice, the sharp and broad peaks could be assigned to the H-bond and octahedral tilt changes, respectively. Then, at lower temperatures, the organic cation undergoes a gradual displacement towards the c-axis, in order to compensate the polarization of the inorganic lattice along the +c-axis. Finally, the role of the inert pair effect (Sn 5s^2) in these changes should not be ignored. The octahedral shape at higher temperatures (>160 K) does not suggest the presence of a localized inert pair. However, at 120 and 140 K the distortion of the SnBr₆ octahedron (Fig. 3c and d) shows conclusive stereochemical evidence of the electron density of the 5s^2 inert pair in the −c direction. Thus, the calorimetric signal at 147 K can be associated with the localization of the inert electron pair. The expected position of the Sn²⁺ inert pair is also shown in Fig. 3c and d.

Thermoelectric properties

Fig. 4 shows the three main thermoelectric properties measured near RT: resistivity (Fig. 4a), the Seebeck coefficient (Fig. 4b) and thermal conductivity (Fig. 4c). The resistivity is around 2×10^3 Ω m at 310 K, a high value that is quite far from being competitive with other materials, such as some halide perovskites.[37] However, this resistivity is better than that reported for lead-containing MAPbBr₃ single-crystals, which is around 10^6 Ω m, and is about the same as the resistivity of Bi-doped samples.[36]
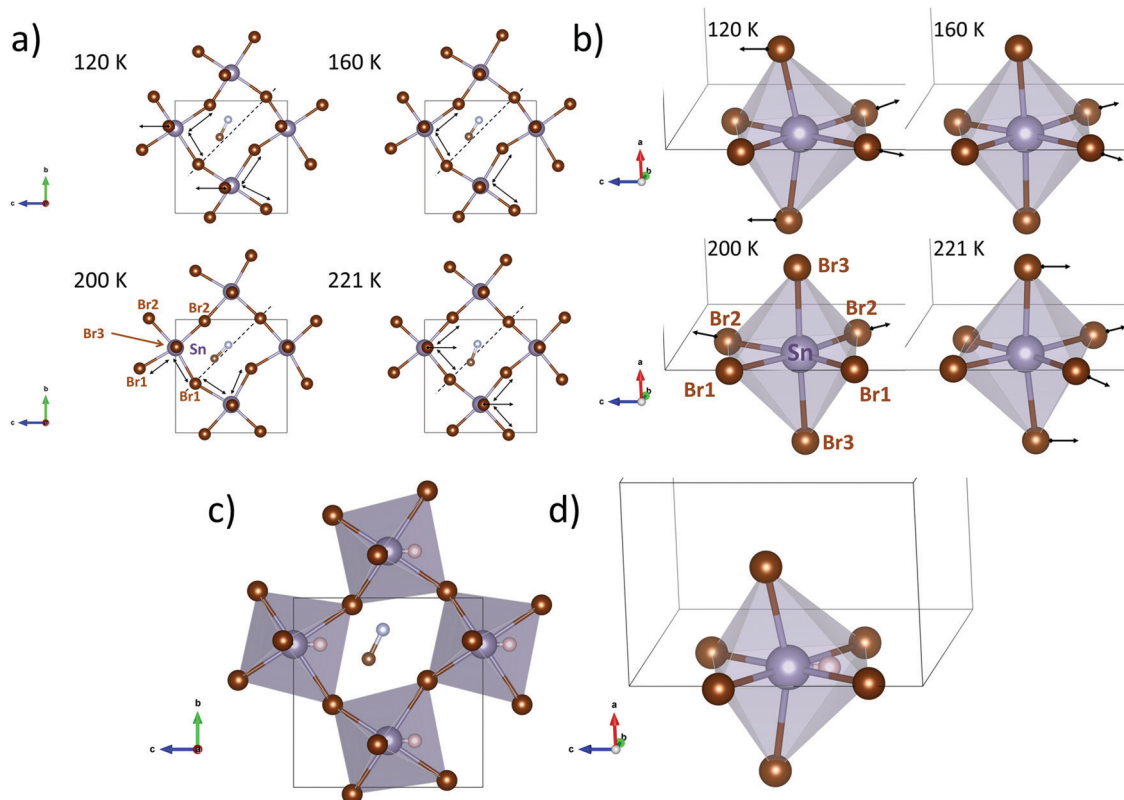
Fig. 3 Crystal structures at selected temperatures along the *a*-axis (a) and the *b*-axis (b). The arrows highlight the bromine displacements in the structure. Crystal structures at 120 K along the *a*-axis (c) and the *b*-axis (d) where the expected position of the tin inert pair is indicated as a white sphere.
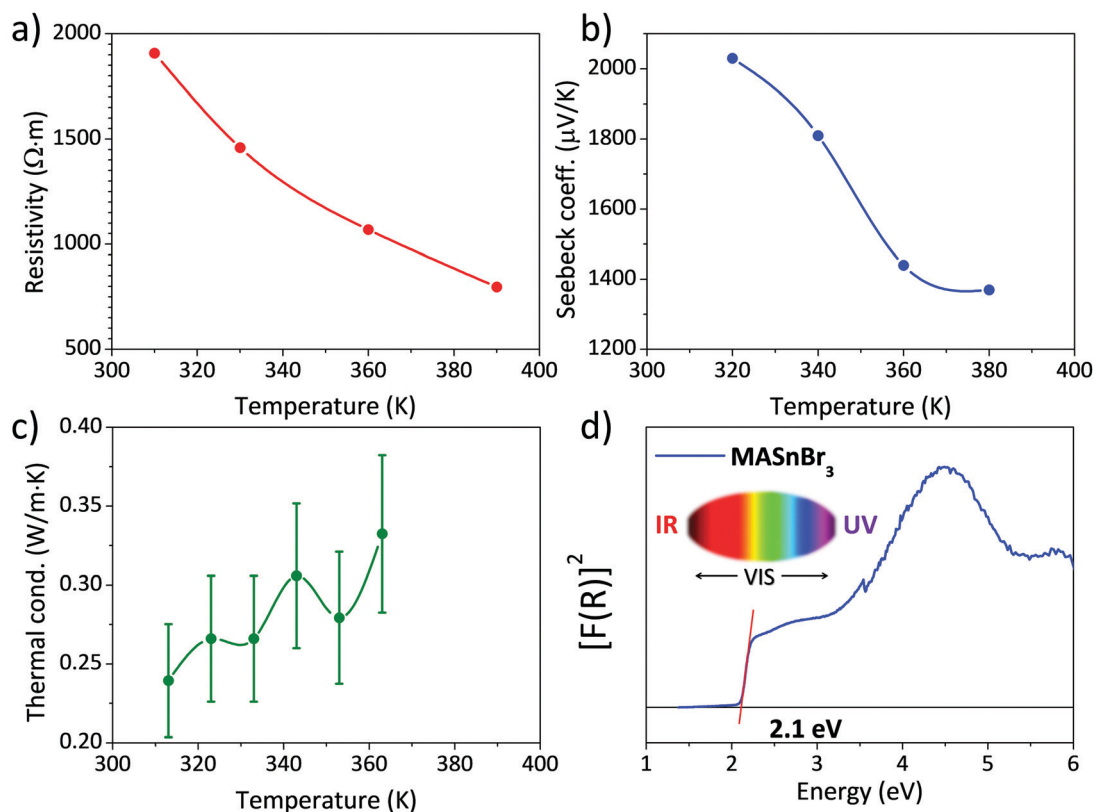

Fig. 4 (a) Electrical resistivity, (b) Seebeck coefficient, (c) thermal conductivity and (d) UV–Vis absorption spectrum of MASnBr$_3$.

The Seebeck coefficient shows a value of $S = 2030$ μV K^{-1} at 320 K. This value is about one order of magnitude higher than that reported for other halide perovskites like $CsSnBr_3$ and hybrid perovskites like $MAPbBr_3$.[36,37] It is also higher than some results obtained from theoretical predictions,[33] calculated for a hole concentration of 1×10^{18} cm^{-3}, and projecting a value around $S = 300$ μV K^{-1} at 300 K. Both the resistivity and Seebeck coefficient decrease with temperature, which could be the effect of the activation of minority carriers.

The thermal conductivity κ is, on the other hand, lower than that reported for other halide and hybrid perovskites,[36,37] and always remains below 0.35 W m·K^{-1} at all the measured temperatures. Combining these values in a zT figure of merit, defined as $zT = S^2\sigma T/\kappa$, yields $zT = 3 \times 16 \cdot 10^{-6}$ at 313 K, which is low compared with state-of-the-art thermoelectric materials, but is superior to other values given for hybrid perovskites, like Bi-doped $MAPbBr_3$, of 1.8×10^{-6}.[36]

Optical gap by UV-Vis spectra

The absorption capacity of $MASnBr_3$ perovskite powder was investigated by diffuse reflectance UV/Vis spectroscopy. Fig. 4d depicts the optical absorption coefficient related to the Kubelka–Munk function $(F(R) = a = (1 - R)^2/2R$, where R is the reflectance versus wavelength in eV).

The band gap for this perovskite at RT has been calculated by extrapolating the linear region to the abscissa. The value obtained for $MASnBr_3$ ($\sim$2.1 eV) agrees with data reported in the literature (2.15 eV[50] or 2.2–2.3 eV[34]), being even slightly smaller, which would improve light absorption. This difference could be related, once more, to the preparation procedure of the present specimen, by mechano-synthesis, as opposed to conventional synthesis techniques by co-evaporation[34] or solution chemistry.[50]

Chemical stability

Fig. 5 shows three XRD patterns of MASbBr3, freshly prepared by ball milling, after 9 days and after 14 days of air exposure under laboratory conditions (typically 40% humidity). The pattern of the fresh sample corresponds to the above-described cubic perovskite stable at RT; the patterns after 9 and 14 days are strongly degraded, with just some of the strong perovskite peaks visible (shown as asterisks). Even visually, some days after the sample was synthesized, the characteristic dark red colour became cream and finally white. The products are identified as the hydrates of methylammonium and tin bromides. These results are just included to highlight the great reactivity and instability of the hybrid perovskite under laboratory conditions, which would require adequate protection against the atmosphere in eventual devices.

Conclusions

$CH_3NH_3SnBr_3$ hybrid perovskite has been successfully prepared as a well-crystallized powder by mechano-chemical synthesis under an inert atmosphere. The crystal structure evolution has been revisited from high angular resolution SXRD data. A complex progression is identified, including four phases, including one cubic, C (at, and immediately below RT) and three orthorhombic crystal structures, O1, O2 and O3. The C, O1 and O2 phases coexist in the 240–200 K range, in contrast with the previous results. The three orthorhombic phases are defined in the acentric $Pmc2_1$ space group, although they exhibit very different unit-cell parameters. This evolution is the result of an interplay between the octahedral tilting of the inorganic framework and the reconstruction of H–Br hydrogen bonds with the organic moiety, yielding the main calorimetric events (224 and 147 K) detected by C_p and DSC measurements. The shape of the $SnBr_6$ octahedra at higher temperatures ($>$160 K) does not denote the presence of the localized $5s^2$ inert pair of the Sn^{2+} ion. However, at 120 and 140 K its distortion indicates conclusive stereochemical evidence of the electron density of the $5s^2$ inert pair in the $-c$ direction. Thus, the calorimetric signal at 147 K can be associated with the localization of the inert electron pairs, which can be identified from the structural features. The optical gap of this specimen synthesized by solvent-free mechano-chemistry, of 2.1 eV, is slightly below the values reported for wet-chemistry prepared materials. The thermoelectric properties are appealing, regarding a large Seebeck coefficient and a low thermal conductivity, although the large electrical resistivity leads to negligible figure of merit values. The great reactivity and instability of this hybrid perovskite under laboratory conditions leads to rapid degradation in a humid environment, thus requiring adequate protection against the atmosphere in devices.
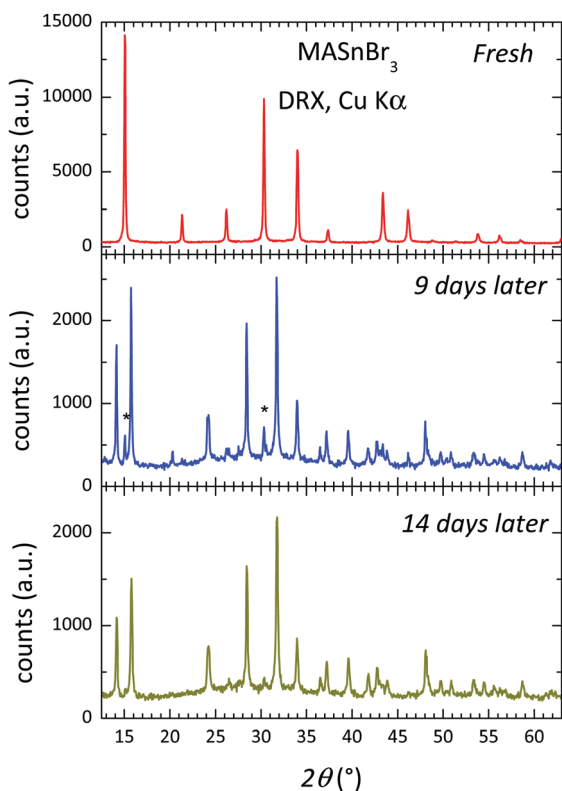

Fig. 5 X-Ray patterns of the fresh sample and after 9 and 14 days.

Conflicts of interest

There are no conflicts to declare.

Acknowledgements

References

1 M. Grätzel, *J. Photochem. Photobiol., C*, 2003, **4**, 145–153.

2 M. A. Green, A. Ho-Baillie and H. J. Snaith, *Nat. Photonics*, 2014, **8**, 506–514.

3 J. Burschka, N. Pellet, S.-J. Moon, R. Humphry-Baker, P. Gao, M. K. Nazeeruddin and M. Grätzel, *Nature*, 2013, **499**, 316–319.

4 T. M. Brenner, D. A. Egger, L. Kronik, G. Hodes and D. Cahen, *Nat. Rev. Mater.*, 2016, **1**, 15007.

5 H. J. Snaith, *J. Phys. Chem. Lett.*, 2013, **4**, 3623–3630.

6 N.-G. Park, *J. Phys. Chem. Lett.*, 2013, **4**, 2423–2429.

7 L. Etgar, P. Gao, Z. Xue, Q. Peng, A. K. Chandiran, B. Liu, M. K. Nazeeruddin and M. Grätzel, *J. Am. Chem. Soc.*, 2012, **134**, 17396–17399.

8 H.-S. Kim, C.-R. Lee, J.-H. Im, K.-B. Lee, T. Moehl, A. Marchioro, S.-J. Moon, R. Humphry-Baker, J.-H. Yum, J. E. Moser, M. Grätzel and N.-G. Park, *Sci. Rep.*, 2012, **2**, 591.

9 H.-Y. Hsu, L. Ji, H. S. Ahn, J. Zhao, E. T. Yu and A. J. Bard, *J. Am. Chem. Soc.*, 2015, **137**, 14758–14764.

10 C. R. Kagan, *Science*, 1999, **286**, 945–947.

11 A. Kojima, M. Ikegami, K. Teshima and T. Miyasaka, *Chem. Lett.*, 2012, **41**, 397–399.

12 P. Gao, M. Grätzel and M. K. Nazeeruddin, *Energy Environ. Sci.*, 2014, **7**, 2448–2463.

13 B. Saparov and D. B. Mitzi, *Chem. Rev.*, 2016, **116**, 4558–4596.

14 G. Niu, X. Guo and L. Wang, *J. Mater. Chem. A*, 2015, **3**, 8970–8980.

15 M. Zhang, H. Yu, M. Lyu, Q. Wang, J.-H. Yun and L. Wang, *Chem. Commun.*, 2014, **50**, 11727–11730.

16 M. C. Alvarez-Galván, J. A. Alonso, C. A. López, E. López-Linares, C. Contreras, M. J. Lázaro, F. Fauth and M. V. Martínez-Huerta, *Cryst. Growth Des.*, 2019, **19**, 918–924.

17 C. A. López, M. C. Álvarez-Galván, M. V. Martínez-Huerta, M. T. Fernández-Díaz and J. A. Alonso, *Chem. – Eur. J.*, 2019, **25**, 4496–4500.

18 C. A. López, M. C. Alvarez-Galván, M. V. Martínez-Huerta, F. Fauth and J. A. Alonso, *CrystEngComm*, 2020, **22**, 767–775.

19 A. Babayigit, A. Ethirajan, M. Muller and B. Conings, *Nat. Mater.*, 2016, **15**, 247–251.

20 F. Sani, S. Shafie, H. Lim and A. Musa, *Materials*, 2018, **11**, 1008.

21 F. Giustino and H. J. Snaith, *ACS Energy Lett.*, 2016, **1**, 1233–1240.

22 C. C. Stoumpos, C. D. Malliakas and M. G. Kanatzidis, *Inorg. Chem.*, 2013, **52**, 9019–9038.

23 F. Hao, C. C. Stoumpos, D. H. Cao, R. P. H. Chang and M. G. Kanatzidis, *Nat. Photonics*, 2014, **8**, 489–494.

24 N. K. Noel, S. D. Stranks, A. Abate, C. Wehrenfennig, S. Guarnera, A.-A. Haghighirad, A. Sadhanala, G. E. Eperon, S. K. Pathak, M. B. Johnston, A. Petrozza, L. M. Herz and H. J. Snaith, *Energy Environ. Sci.*, 2014, **7**, 3061–3068.

25 S. F. Hoefler, G. Trimmel and T. Rath, *Monatshefte für Chemie – Chem. Mon.*, 2017, **148**, 795–826.

26 K. Yamada, K. Nakada, Y. Takeuchi, K. Nawa and Y. Yamane, *Bull. Chem. Soc. Jpn.*, 2011, **84**, 926–932.

27 K. Yamada, S. Hino, S. Hirose, Y. Yamane, I. Turkevych, T. Urano, H. Tomiyasu, H. Yamagishi and S. Aramaki, *Bull. Chem. Soc. Jpn.*, 2018, **91**, 1196–1204.

28 K. Yamada, K. Fujise, S. Hino, Y. Yamane and T. Nakagama, *Chem. Lett.*, 2019, **48**, 749–752.

29 T. Handa, A. Wakamiya and Y. Kanemitsu, *APL Mater.*, 2019, **7**, 080903.

30 W. Yang, F. Igbari, Y. Lou, Z. Wang and L. Liao, *Adv. Energy Mater.*, 2020, **10**, 1902584.

31 L. M. Herz, *ACS Energy Lett.*, 2017, **2**, 1539–1548.

32 H.-Y. Hsu, L. Ji, M. Du, J. Zhao, E. T. Yu and A. J. Bard, *Electrochim. Acta*, 2016, **220**, 205–210.

33 A. Shukla, V. K. Sharma, S. K. Gupta and A. S. Verma, *Mater. Chem. Phys.*, 2020, **253**, 123389.

34 M.-C. Jung, S. R. Raga and Y. Qi, *RSC Adv.*, 2016, **6**, 2819–2825.

35 W. Qian, X. Cheng, Y. Zhao, J. Zhou, J. He, H. Li, Q. Xu, N. Li, D. Chen and J. Lu, *Adv. Mater.*, 2019, **31**, 1806424.

36 W. Tang, J. Zhang, S. Ratnasingham, F. Liscio, K. Chen, T. Liu, K. Wan, E. S. Galindez, E. Bilotti, M. Reece, M. Baxendale, S. Milita, M. A. McLachlan, L. Su and O. Fenwick, *J. Mater. Chem. A*, 2020, **8**, 13594–13599.

37 H. Xie, S. Hao, J. Bao, T. J. Slade, G. J. Snyder, C. Wolverton and M. G. Kanatzidis, *J. Am. Chem. Soc.*, 2020, **142**, 9553–9563.

38 K. Yamada, S. Nose, T. Umehara, T. Okuda and S. Ichiba, *Bull. Chem. Soc. Jpn.*, 1988, **61**, 4265–4268.

39 N. Onoda-Yamamuro, T. Matsuo and H. Suga, *J. Chem. Thermodyn.*, 1991, **23**, 987–999.

40 I. Swainson, L. Chi, J.-H. Her, L. Cranswick, P. Stephens, B. Winkler, D. J. Wilson and V. Milman, *Acta Crystallogr., Sect. B: Struct. Sci.*, 2010, **66**, 422–429.

41 F. Fauth, R. Boer, F. Gil-Ortiz, C. Popescu, O. Vallcorba, I. Peral, D. Fullà, J. Benach and J. Juanhuix, *Eur. Phys. J. Plus*, 2015, **130**, 160.

42 H. M. Rietveld, *J. Appl. Crystallogr.*, 1969, **2**, 65–71.

43 J. Rodríguez-Carvajal, *Phys. Rev. B: Condens. Matter Mater. Phys.*, 1993, **192**, 55–69.

44 N. Onoda-Yamamuro, O. Yamamuro, T. Matsuo, H. Suga, K. Oikawa, N. Tsuchiya, T. Kamiyama and H. Asano, *Phys. Rev. B: Condens. Matter Mater. Phys.*, 1995, **213–214**, 411–413.

45 R. E. Wasylishen, O. Knop and J. B. Macdonald, *Solid State Commun.*, 1985, **56**, 581–582.

46 N. Onoda-Yamamuro, T. Matsuo and H. Suga, *J. Phys. Chem. Solids*, 1990, **51**, 1383–1395.

47 C. A. López, M. V. Martínez-Huerta, M. C. Alvarez-Galván, P. Kayser, P. Gant, A. Castellanos-Gomez, M. T. Fernández-Díaz, F. Fauth and J. A. Alonso, *Inorg. Chem.*, 2017, **56**, 14214–14219.

48 L. H. Ahrens, *Geochim. Cosmochim. Acta*, 1952, **2**, 155–169.

49 R. D. Shannon, *Acta Crystallogr. Sect. A*, 1976, **32**, 751–767.

50 B. Li, R. Long, Y. Xia and Q. Mi, *Angew. Chem., Int. Ed.*, 2018, **57**, 13154–13158.